

铝含量对激光增材制造 TC4 合金组织及性能的调控

葛禄成, 赵紫松, 刘宁夏, 梁彦鹏, 张静涛, 王存山*

大连理工大学三束材料改性教育部重点实验室, 辽宁 大连 116024

摘要 为提升激光增材制造 TC4 合金的综合性能, 采用铝为合金化组元对其进行组织与性能调控。结果表明: 在激光增材制造的非平衡凝固条件下, 不同铝添加量的 TC4 合金凝固组织皆由呈交错排列的 β -Ti 和 α -Ti 网篮组织构成, 但有所不同的是, 随着铝添加量的增加, 组织中 α -Ti 固溶体的相对含量逐渐增多, 其尺寸呈现出先减后增的变化趋势, 即在铝添加量(质量分数)为 1.5% 时达到最小。沉积态合金的硬度、屈服强度和摩擦磨损性能随着铝添加量的增加而逐渐增大, 而塑性、耐腐蚀性和表面粗糙度则分别在铝添加量(质量分数)为 1.5% 时达到最优。这表明, 添加 1.5% Al 的沉积态合金有着最佳的性能匹配, 其力学性能、摩擦学性能、电化学性能和成形性能均较 TC4 合金有了明显提升。

关键词 激光技术; 激光增材制造; TC4 合金; 成分调控; 组织; 性能

中图分类号 TG401 **文献标志码** A

doi: 10.3788/CJL202148.1402004

1 引言

金属零件的激光增材制造技术是基于分层叠加及逐层堆积的快速成形原理, 以金属粉末为原料, 在零件三维模型离散切片数据的直接驱动下, 通过高功率激光进行逐层沉积, 直接制造出具有复杂结构的高性能零件^[1]。该技术兼具快速成形和激光熔覆的优势, 具有效率高、灵活性好、成本低以及性能和成形性可控等优点, 为制造几何形状复杂的高致密零件提供了一种新的加工方法^[2-6]。

TC4 合金具有综合力学性能优异和耐腐蚀性好等优点, 已被广泛应用于生物医学、航空航天、汽车、石油化工等领域^[7-10], 近年来受到了国内外激光增材制造研究人员的广泛关注, 并在微观组织演化、工艺与过程控制、冶金缺陷调控等方面取得了重要研究进展^[11-18]。然而, 该合金最初是为了满足航空需求设计而开发的, 并未考虑激光增材制造复杂的物理冶金过程的特殊性, 其低的热稳定性极易使其在激光增材制造的多周期和强约束热循环过程中发生局域固态相变, 形成介稳定相, 从而对力学性能的

均匀性控制带来很大困难^[19-20]。因此, 需要严格控制激光增材制造工艺并采取适当的后续热处理予以调控。尤为重要的是, 该合金对冶金缺陷的敏感性较高, 极易在成形零件内部产生气孔, 以及在搭接区发生熔合不良现象, 甚至因合金低的抗裂强度, 在热应力、组织应力和拘束应力的综合作用下诱发裂纹的产生, 需采用内应力离散控制等特殊方法予以防控^[21-25]。因此, 利用合金化对 TC4 合金的组织 and 性能进行有效调控, 对于满足其激光增材制造工艺性和使用性要求具有重要意义。

通过对 TC4 合金成分进行解析可知, 钒是钛的 β 同晶元素, 其在 β -Ti 中能无限固溶, 在 α -Ti 中也有一定的溶解度。因此, 钒能起到有效的固溶强化作用, 且在提高合金强度的同时还能使合金保持良好的塑性^[26]。然而, 钒的加入会扩大液固凝固区间, 增加合金对冶金缺陷的敏感性, 因此需要严格控制钒的含量。铝是 α 相稳定元素, 其主要溶入合金 α 固溶体中, 只有少量溶于 β 相中, 具有显著的固溶强化效果, 可以提高合金的强度, 且在铝质量分数低于 7% 时不会显著降低合金的塑性, 同时能增强 α 相中

收稿日期: 2020-11-23; 修回日期: 2020-12-01; 录用日期: 2021-01-13

基金项目: 国家重点研发计划(2016YFB1100103)、国家自然科学基金(51371041)

通信作者: *laser@dlut.edu.cn

的原子间结合力,提升钛合金的热稳定性。鉴于此,本文以 TC4 合金为基础成分,以铝为合金化组元,采用增材制造工艺制备了铝含量不同的 TC4 合金,研究了合金的凝固组织和性能随铝含量的变化,以实现合金成分的优化,提升 TC4 合金的力学、化学、摩擦学和工艺学性能。

2 试验材料与方法

为使基体和沉积层实现良好的冶金结合,避免冶金缺陷的产生,本次试验选取与沉积层成分相同的 TC4 合金作为基体材料,其尺寸为 $20\text{ mm} \times 20\text{ mm} \times 10\text{ mm}$ 。选取雾化法制备的 TC4 合金粉末作为基质材料,其平均粒度约为 $48\text{ }\mu\text{m}$ 。选取纯度为 99.90%、粒度约为 $75\text{ }\mu\text{m}$ 的纯铝粉为合金化组元,其添加量为 0.5%~3.0% (质量分数)。首先按照配比进行称重,然后将混合粉末置于真空球磨机中,在 200 r/min 的转速下球磨 6 h,以混合均匀的粉末作为激光增材制造粉末。最后,采用 5 kW 横流 CO_2 激光增材制造系统,按照双向扫描策略逐层制备尺寸为 $15\text{ mm} \times 15\text{ mm} \times 12\text{ mm}$ 的沉积体。基于前期的工艺探索,以沉积层组织和成形质量为评判标准,选择优化的工艺参数(激光功率 2 kW,激光束直径 4 mm,搭接率 50%,扫描速度 5 mm/s,单层铺粉厚度 0.5 mm,氩气流量 8.0 L/min)进行激光增材制造。

增材制造完成后,采用线切割沿垂直于激光扫描方向切割激光沉积试样,然后进行打磨和抛光,将其制备成金相试样。采用 XRD-6000 型 X 射线衍射(XRD)仪对金相试样进行物相鉴定,所用辐射源为 $\text{Cu K}\alpha$,操作电压和电流分别为 40 kV 和 40 mA。采用 Zeiss Supra 55 型扫描电镜(SEM)对经 7% (体积分数) $\text{HF} + 73\% \text{ HNO}_3 + 20\% \text{ H}_2\text{O}_2$ 腐蚀液浸蚀的金相试样进行组织形貌观察。为鉴别沉积层中析出相的类型,采用 G220 S-Twin 型透射电子显微镜(TEM)对其进行选区电子衍射分析。采用 HVS-5Z 型显微硬度测试计以 4.9 N 的压痕载荷和 15 s 的保荷时间对沉积层的显微硬度进行测试。为了获得较为准确的数据,每种成分的沉积态合金按“井”字形测试 30 点,并取 30 点的均值作为最终的显微硬度值。室温压缩试验在 DNS100 型万能试验机上进行,压缩试样尺寸为 $\Phi 3\text{ mm} \times 6\text{ mm}$,测试时的应变速率为 0.036 mm/min 。沉积态合金的干滑动摩擦磨损性能在 CETRUMT-2 型往复摩擦磨损试验机上进行。测试时以直径为 5 mm、硬度为

55 HRC 的 GCr15 球为摩擦副,单向滑移距离为 5 mm,施加的法向载荷为 5 N,滑移速度为 2 mm/s。采用 CorrTest 电化学工作站对沉积态合金在 1 mol/L 的 HCl 溶液中进行电化学性能测试,选用饱和甘汞作为参比电极,Pt 作为辅助电极。采用 OLYMPUS 型激光共聚焦扫描显微镜测试沉积态合金的表面粗糙度。

3 试验结果与分析

3.1 显微组织

图 1 所示为添加不同铝含量的激光增材制造 TC4 合金的 XRD 图谱。可见,沉积态 TC4 合金由 $\beta\text{-Ti}$ 、 $\alpha\text{-Ti}/\alpha'\text{-Ti}$ 固溶体(二者的衍射花样十分相近,而无法利用 XRD 予以鉴别)组成。当在 TC4 合金中添加质量分数为 0.5%~3.0% 的铝时,合金的相组成并未改变,仍由 $\beta\text{-Ti}$ 、 $\alpha\text{-Ti}/\alpha'\text{-Ti}$ 固溶体组成。但基于直接对比法的计算表明,随着合金中稳定 α 相——铝元素的质量分数由 0% 增加到 0.5%、1.0%、1.5%、2.0%、3.0%,组织中 $\alpha\text{-Ti}/\alpha'\text{-Ti}$ 固溶体的相对含量(体积分数)逐渐由 99.65% 增加到 99.66%、99.69%、99.74%、99.83%、99.84%。与此同时,因原子半径较小的铝元素在 $\alpha\text{-Ti}/\alpha'\text{-Ti}$ 中固溶量的增加, $\alpha\text{-Ti}/\alpha'\text{-Ti}$ 固溶体所对应的衍射峰逐渐向高衍射角方向偏移。其结果是该固溶体的晶格常数 c 逐渐增大,而晶格常数 a 有所减小(如表 1 所示),这预示着铝元素更倾向于占据空间点阵的 $\{1100\}$ 晶面。

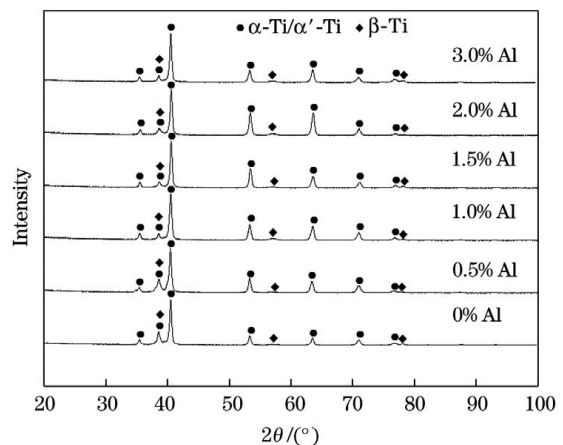


图 1 不同铝添加量沉积态合金的 XRD 图谱

Fig. 1 XRD patterns of as-deposited alloys with different Al additions

图 2 所示为不同铝添加量沉积态合金的典型 SEM 形貌。由图 2(a)可见,沉积态 TC4 合金组织呈现出明显的网篮状形貌特征,即在 $\beta\text{-Ti}$ 晶粒内部

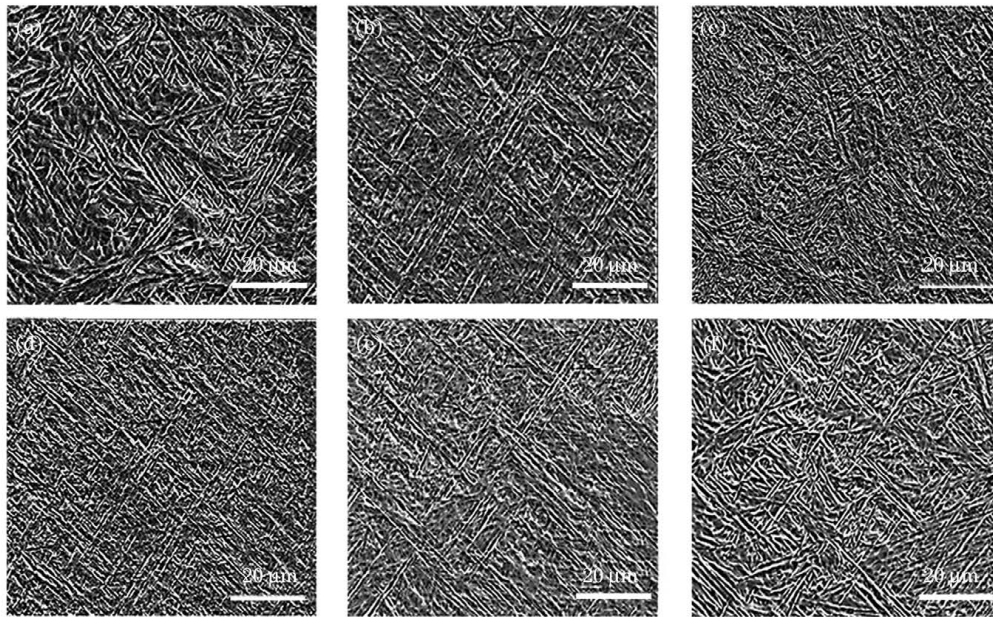


图 2 不同铝添加量沉积态合金典型的 SEM 形貌。(a) 0% Al; (b) 0.5% Al; (c) 1.0% Al; (d) 1.5% Al; (e) 2.0% Al; (f) 3.0% Al

Fig. 2 Typical SEM morphologies of as-deposited alloys with different Al additions. (a) 0% Al; (b) 0.5% Al; (c) 1.0% Al; (d) 1.5% Al; (e) 2.0% Al; (f) 3.0% Al

分布着交错排列的 α -Ti/ α' -Ti 固溶体。为了鉴别晶粒内析出相的类型,采用 TEM 对其结构进行了分析。

表 1 不同铝添加量沉积态合金组成相的晶格常数
Table 1 Lattice parameters of constituent phases in as-deposited alloys with different Al additions

Al addition (mass fraction) /%	a_{α} / nm	c_{α} / nm	a_{β} / nm
0	0.2862	0.4674	0.3305
0.5	0.2861	0.4676	0.3304
1.0	0.2861	0.4682	0.3304
1.5	0.2859	0.4689	0.3305
2.0	0.2858	0.4694	0.3303
3.0	0.2854	0.4701	0.3302

由图 3(a)所示 TEM 明场像可以清晰地看到明亮板条相与深色基体相呈现出明显的层状分布特征,且不同取向的集束相互交错,构成了网篮状组织。通过对明亮板条相进行多处选区电子衍射分析可知,该相为具有密排六方结构的 α -Ti 固溶体,其代表性电子衍射花样如图 3(b)所示。当在 TC4 合金中添加质量分数为 0.5%~3.0% 的铝后,合金凝固组织仍保持网篮状形貌特征,如图 2(b)~(f)所示。但大量的视场统计分析表明,随着铝添加量的增加,组织中 α -Ti 固溶体的尺寸呈现出先减小后增大的变化趋势,即在添加铝的质量分数为 1.5% 时, α -Ti 固溶体的晶粒尺寸最小。根据金属学理论,析出相的尺寸与初生相的晶粒尺寸密切相关,而初生相的晶粒尺寸又取决于其凝固区间。通常来说,凝

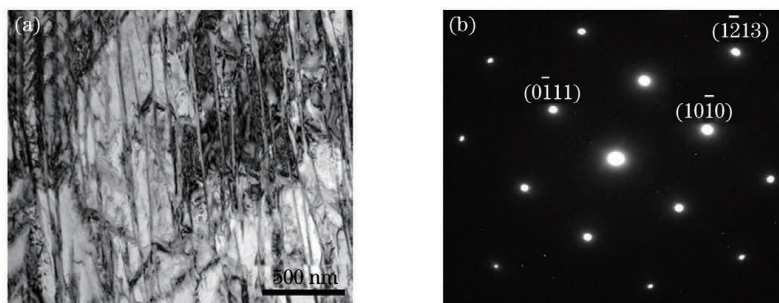


图 3 沉积态 TC4 合金的 TEM 图。(a) 明场像; (b) 选区电子衍射花样

Fig. 3 TEM images of as-deposited TC4 alloy. (a) Bright-field image; (b) electron diffraction pattern

固区间越窄,初生相的凝固时间越短,其晶粒越细小,析出相的尺寸也将随之减小。为此,利用 JMatPro 软件对合金的凝固区间进行了计算。计算结果表明,合金凝固区间随铝添加量的变化趋势与 α -Ti 的大小随铝添加量的变化趋势十分吻合(如图 4 所示),这很好地诠释了 α -Ti 尺寸的上述变化。

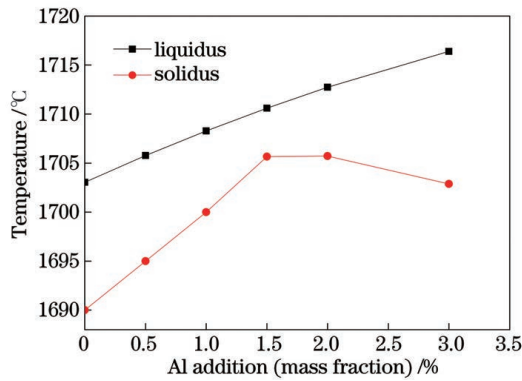


图 4 沉积态合金凝固区间随铝添加量的变化曲线
Fig. 4 Variation of solidification temperature range of as-deposited alloys with Al additions

3.2 力学性能

图 5 所示为沉积态合金平均显微硬度随铝添加量的变化曲线。随着铝添加量的增加,在 α -Ti 相对含量增加和固溶强化这两个主控因素的影响下,沉积态合金的平均显微硬度逐渐增加。

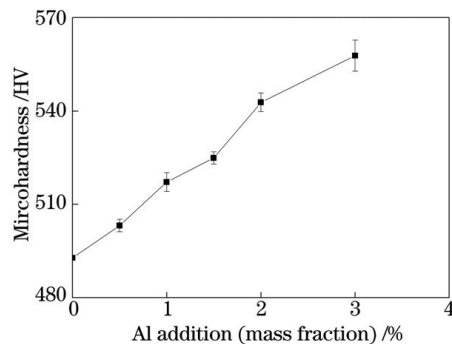


图 5 沉积态合金显微硬度随铝添加量的变化曲线
Fig. 5 Variation of microhardness of as-deposited alloys with Al additions

图 6 所示为添加不同铝含量沉积态合金的室温压缩应力-应变曲线。可见:所有沉积态合金皆呈现出典型的塑性材料的压缩变形特性,即在最大许用应力下只经历线性弹性变形和非线性塑性变形,而未发生压缩断裂;但有所不同的是,随着铝添加量的增加,沉积态合金的屈服强度($\sigma_{0.2}$)、25%应变所对应的抗压强度(σ_{25})逐渐增大,而相对压缩率(H)则呈先增加后减小的变化趋势,其在铝添加量(质量分数)为 1.5% 时达到最大(如表 2 所示)。这表明添

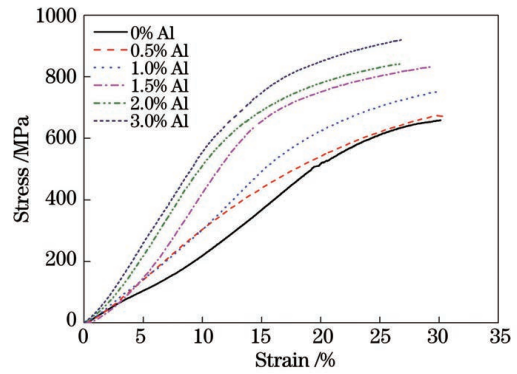


图 6 不同铝添加量沉积态合金的压缩应力-应变曲线图
Fig. 6 Compressive stress-strain curves of as-deposited alloys with different Al additions

表 2 不同铝添加量沉积态合金的压缩试验数据
Table 2 Compressive test data of as-deposited alloys with different Al additions

Al addition (mass fraction) / %	$\sigma_{0.2}$ / MPa	σ_{25} / MPa	H / %
0	538.61	610.85	7.76
0.5	552.09	622.75	9.43
1.0	626.51	703.71	10.41
1.5	695.59	803.54	16.37
2.0	724.52	828.78	13.02
3.0	812.13	904.82	11.85

加适量铝可以实现合金强度与塑性的良好匹配。

采用扫描电镜对压缩试样进行观察后发现,在其侧面存在着许多沿最大剪切应力方向分布的滑移带,且这些滑移带被严格限制在 α -Ti 板条间很短的距离内,未发现有滑移传输现象的发生。随着铝添加量的增加,滑移带间距逐渐减小,滑移带数量有所增加,甚至在局部变形区出现了与一次滑移带呈 60° 交角的二次滑移带。与此同时,因在 α/β 相界面处大的应力集中,局部微区形成了沿相界方向延展的微裂纹。上述两种典型的侧表面形貌如图 7 所示。

根据金属塑性变形理论,体心立方结构相较于密排六方结构相有更多的滑移系,故在变形过程中滑移首先发生在 β -Ti 固溶体中。当位错滑移至 α/β 相界面时,因二者迥异的结构和大的取向差,滑移不能从 β 相直接延续至 α 相中,从而在相界面产生位错塞积,使 β 相的继续变形受阻,进而导致了合金的强化。这种强化方式与 α 相的数量密切相关,即 α 相的数量越多,位错滑移的阻力越大,且随着 α 相晶格畸变的增加,其产生的附加应变场会进一步增大位错滑移的阻力,甚至会施加反向应力作用于位错源,

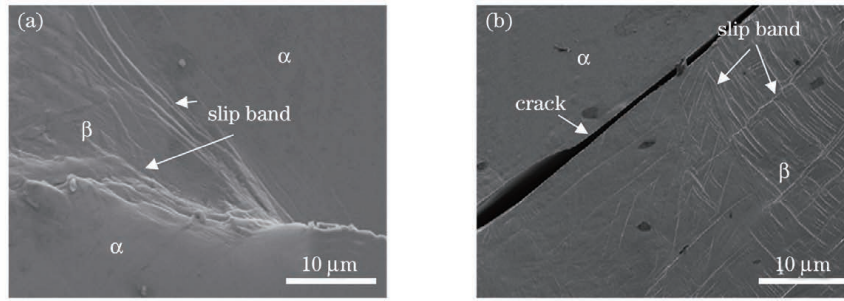


图 7 沉积态合金两种典型的侧表面形貌。(a) 1.0% Al; (b) 2.0% Al

Fig. 7 Two typical lateral surface images of as-deposited alloys. (a) 1.0% Al; (b) 2.0% Al

诱发 β 相发生二次滑移,使流变应力迅速提高。这很好地诠释了为什么合金强度会随着铝添加量的增加而逐渐提高。合金的塑性在很大程度上取决于 α 相的尺寸。厚的 α 板条变形时易发生断裂,在局部区域形成一些沿板条长轴方向扩展的微裂纹,而薄的 α 板条则能承受一定的变形;因此,与 α 相尺寸随铝添加量变化趋势相对应,合金的塑性也呈现出先增后减的变化趋势,即当铝添加量(质量分数)为 1.5% 时,沉积态合金有着最佳的塑性。

3.3 摩擦磨损性能

图 8 为干摩擦磨损条件下沉积态合金摩擦因数和磨痕宽度随铝添加量的变化曲线。可见,随着铝添加量的增加,沉积态合金的摩擦因数和磨痕宽度逐渐减小,即增大铝的添加量有利于提高合金的减摩性和耐磨性。

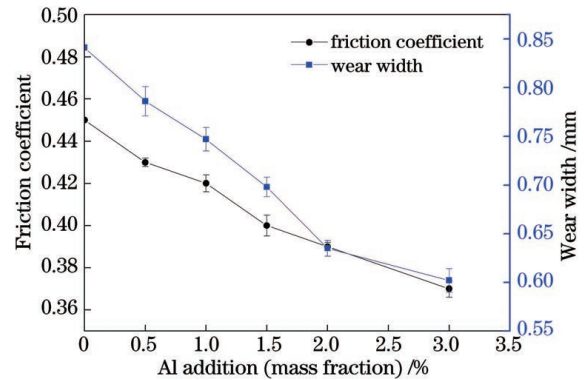


图 8 沉积态合金摩擦因数和磨痕宽度随铝添加量的变化
Fig. 8 Variations of friction coefficient and wear width of as-deposited alloys with Al additions

为了揭示沉积态合金的摩擦磨损机理,采用 SEM 对磨损表面进行了观察。由图 9 可见,不同铝

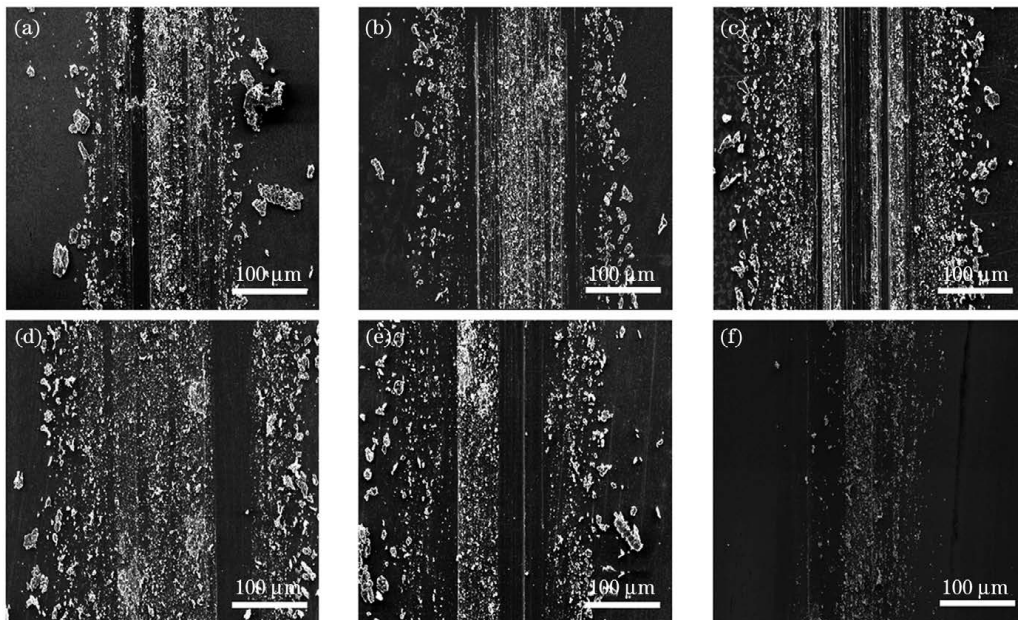


图 9 不同铝添加量沉积态合金的磨损表面形貌。(a) 0% Al; (b) 0.5% Al; (c) 1.0% Al; (d) 1.5% Al; (e) 2.0% Al; (f) 3.0% Al

Fig. 9 Worn surface morphologies of as-deposited alloys with different Al additions. (a) 0% Al; (b) 0.5% Al; (c) 1.0% Al; (d) 1.5% Al; (e) 2.0% Al; (f) 3.0% Al

含量沉积态合金的磨损表面皆呈现出表征磨粒磨损特征的犁沟。但有所不同的是,随着铝添加量增加,沉积态合金的硬度提高,从而有效地增强了合金的抗磨粒磨损能力,使得犁沟逐渐变浅变窄,合金的耐磨性也随之增加。与此同时,沉积态合金与 GCr15 钢之间低的原子结合力,使得它们在干摩擦磨损过程中不易发生黏着现象,且沉积态合金的硬度随着铝添加量的增加而提高,因此摩擦副间的接触由起始的微凸点接触迅速变为平滑的面接触,降低了二者之间的剪切阻力,从而使得沉积态合金的减摩性呈现出递增的变化趋势。

3.4 耐蚀性

图10所示为不同铝添加量沉积态合金在HCl

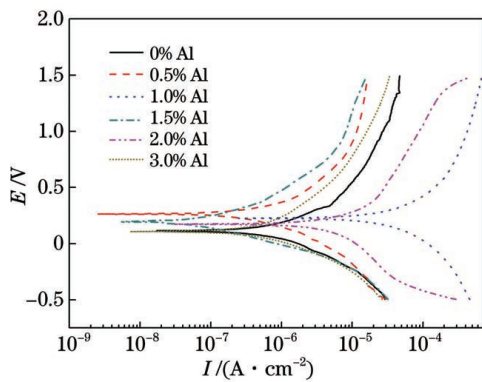


图 10 不同铝添加量沉积态合金在 HCl 溶液中的动电位极化曲线

Fig. 10 Potentiodynamic polarization curves of as-deposited alloys in HCl solution

溶液中的动电位极化曲线。可见,不同铝添加量的沉积态合金有着相似的极化曲线,皆经历了活化溶解、活化钝化和稳定钝化三个阶段,但电化学参量却存在着明显差异。由表 3 所示的利用塔菲尔外推法求得的自腐蚀电位和自腐蚀电流密度可以看出,沉积态合金的自腐蚀电位(E_{corr})随着铝添加量的增加而逐渐增大,并在铝添加量(质量分数)为 1.5% 时达到最大,而后开始逐渐降低,而自腐蚀电流密度(I_{corr})则呈现出相反的变化趋势。由此可以得出,添加 1.5% Al 的沉积态合金具有最好的耐蚀性。

表 3 不同铝添加量沉积态合金在 HCl 溶液中的耐蚀性

Table 3 Corrosion resistance in HCl solution for as-deposited alloys with different Al additions

Al addition (mass fraction) /%	$I_{corr} /$ ($10^{-7} \text{ A} \cdot \text{cm}^{-2}$)	E_{corr} (versus SCE) /V
0	9.980	0.11503
0.5	9.741	0.19411
1.0	4.525	0.22681
1.5	1.256	0.26424
2.0	3.544	0.17397
3.0	5.566	0.10918

图 11 是在 SEM 下观察到的不同铝添加量沉积态合金表面的腐蚀形貌。可见,不同铝添加量沉积态合金的腐蚀表面皆呈现出因活性溶解而导致的刻蚀结构。这是因为在由 β -Ti 和 α -Ti 两相构成的

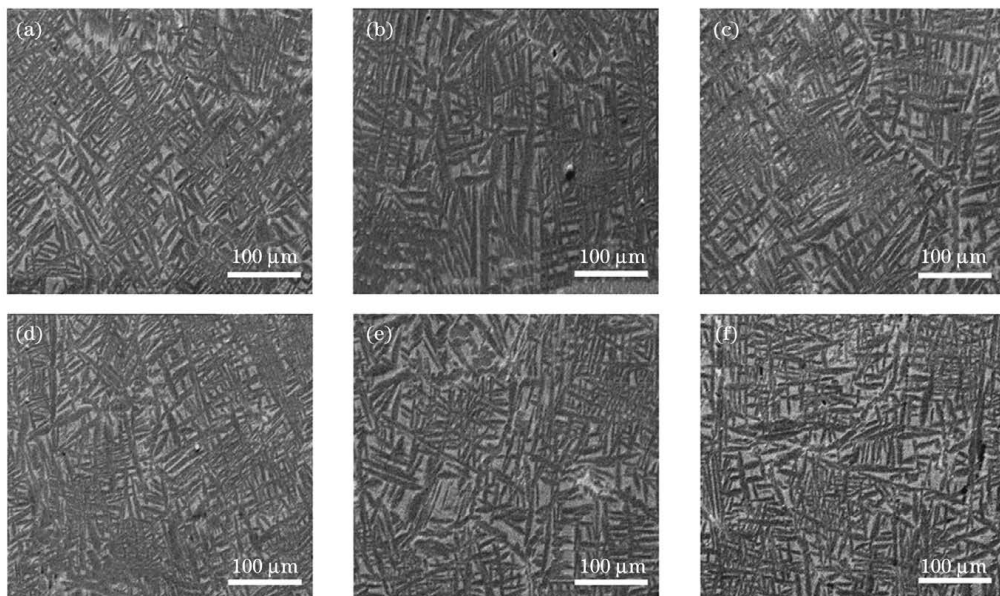


图 11 不同铝添加量沉积态合金表面的腐蚀形貌。(a) 0% Al; (b) 0.5% Al; (c) 1.0% Al; (d) 1.5% Al; (e) 2.0% Al; (f) 3.0% Al

Fig. 11 Corroded surface morphologies of as-deposited alloys with different Al additions. (a) 0% Al; (b) 0.5% Al; (c) 1.0% Al; (d) 1.5% Al; (e) 2.0% Al; (f) 3.0% Al

组织中, β -Ti 的电极电位要较 α -Ti 的电极电位高, 二者在 HCl 溶液中会构成原电池, 其中 β -Ti 为阴极, 而 α -Ti 为阳极。因此, α -Ti 将优先被腐蚀, 致使腐蚀表面留下了 β -Ti 浮凸。随着铝添加量的增加, 一方面组织中 α -Ti 的相对含量逐渐增加, 有降低沉积态合金耐蚀性的趋势, 另一方面, 组织中 α -Ti 相的尺寸呈现出先减后增的变化趋势。晶粒的大小是影响材料耐蚀性的重要因素之一。通常而言, 细小的板条状组织要较粗大的板条状组织具有更好的耐蚀性, 因为前者在腐蚀过程中会产生“屏蔽效应”, 降低电偶腐蚀, 提升合金的耐腐蚀能力。在上述二种因素的综合作用下, 沉积态合金的耐蚀性呈现出先增后减的变化趋势, 即沉积态合金中 α -Ti 的数量和尺寸对合金的耐蚀性起着十分关键的作用, 低体积分数和小尺寸的 α -Ti 有助于提升合金的耐蚀性。

3.5 表面粗糙度

图 12 为沉积态合金表面粗糙度 (R_a) 随铝添加量的变化曲线。可见, 随着铝添加量的增加, 沉积态合金的表面粗糙度逐渐减小, 并在铝添加量 (质量分数) 为 1.5% 时达到最小, 而后开始缓慢增加。在工艺参数一定的情况下, 合金表面粗糙度主要与熔体的流动性和铺展性有关。

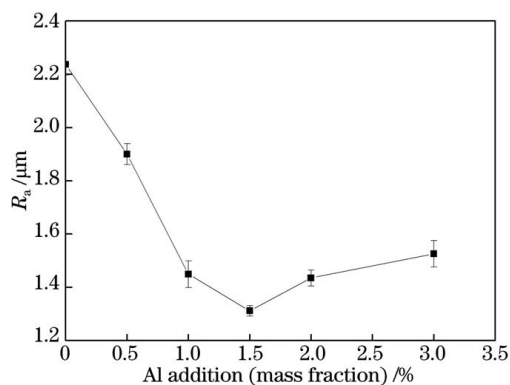


图 12 沉积态合金表面粗糙度随铝添加量的变化曲线
Fig. 12 Variation of surface roughness of as-deposited alloys with Al additions

按照金属凝固学原理, 液态合金的流动性与合金液固凝固区间密切相关, 即液固凝固区间越窄, 液态合金的流动性越好^[27]。基于此, 并结合图 4 所示的合金液固凝固区间随铝添加量的变化关系, 可以推断合金的液态流动性随着铝添加量增加呈现出先增后减的变化趋势, 在铝添加量 (质量分数) 为 1.5% 时液态合金的流动性为最佳。表面张力是熔池内流体流动的主要驱动力, 其直接影响液态合金

的铺展性。而表面张力又与熔池的温度梯度密切相关, 即降低熔池的温度梯度, 就会降低熔池的表面张力, 从而增加合金的铺展性。具体到本研究中的合金体系, 随着高导热性铝元素的增加, 势必会因熔池温度梯度的降低而提升液态合金的铺展性。为此, 本课题组采用与沉积层相同的工艺参数制备了单道熔覆层, 并对其与 TC4 基材所形成的接触角进行测试 (接触角是在熔覆层边缘与基体表面接触处, 作熔覆层表面的切线和基体表面的切线, 这两条切线在熔覆层内部所成的夹角)。结果表明, 随着铝添加量 (质量分数) 由 0% 增加到 0.5%、1.0%、1.5%、2.0%、3.0%, 单道熔覆层与 TC4 基材接触角由 45° 依次降至 42°、40°、38°、33° 和 29°, 这充分验证了上述结论的正确性。正是上述两种因素的综合作用, 才导致添加 1.5% Al 的合金有着最低的表面粗糙度。

4 结 论

XRD、SEM 和 TEM 分析表明, 不同铝添加量的沉积态 TC4 合金皆由 β -Ti 和 α -Ti 呈交错排列的网篮组织构成, 且随着铝添加量 (质量分数) 由 0% 增加到 0.5%、1.0%、1.5%、2.0%、3.0%, 凝固组织中的 α -Ti 的含量 (体积分数) 逐渐由 99.65% 增至 99.66%、99.69%、99.74%、99.83%、99.84%, 尺寸呈现先减小后增大的变化趋势, 即在铝添加量为 1.5% (质量分数) 时达到最小。

随着铝添加量的增加, 受 α -Ti 含量增加和固溶强化这两个主控因素的影响, 沉积态合金的硬度、屈服强度和压缩强度逐渐增大, 其值分别为 503.17~557.78 HV、552.09~812.13 MPa、622.75 MPa~904.82 MPa, 较沉积态 TC4 合金分别提高了 2.11%~13.20%、2.50%~50.78% 和 1.94%~48.12%; 而压缩率则呈现先增后减的变化趋势, 即在铝添加量为 1.5% (质量分数) 时达到最高, 压缩率的范围为 9.43%~16.37%, 较沉积态 TC4 合金的压缩率提高了 21.52%~110.95%。

随着铝添加量的增加, 摩擦因数和磨痕宽度呈现出单调递减的变化趋势, 其值分别介于 0.37~0.43 和 0.652~0.786 mm, 减摩性和耐磨性较沉积态 TC4 合金分别提高了 4.44%~17.78% 和 6.54%~28.42%。自腐蚀电流密度和表面粗糙度呈现先降低后增加的变化趋势, 在铝添加量为 1.5% (质量分数) 时分别达到最低, 其值分别在 $1.256 \times 10^{-7} \sim 9.741 \times 10^{-7} \text{ A} \cdot \text{cm}^{-2}$ 和 $1.312 \sim$

1. 900 μm 范围内变动,耐蚀性较沉积态 TC4 合金提高了 2.39%~87.41%,表面粗糙度较沉积态 TC4 合金降低了 15.06%~41.35%。

铝添加量为 1.5%(质量分数)时,沉积态合金可以达到最优的性能匹配,其力学性能、摩擦学性能、电化学性能和成形性能明显优于沉积态 TC4 合金。

参 考 文 献

- [1] Zhang Y W, Zhang S Q, Wang H M. Microstructure and mechanical properties of directional rapidly solidified Ni-base superalloy Rene95 by laser melting deposition manufacturing [J]. *Rare Metal Materials and Engineering*, 2008, 37(1): 169-172.
张亚玮, 张述泉, 王华明. 激光熔化沉积定向快速凝固高温合金组织及性能 [J]. *稀有金属材料与工程*, 2008, 37(1): 169-172.
- [2] Chaudhary V, Mantri S A, Ramanujan R V, et al. Additive manufacturing of magnetic materials [J]. *Progress in Materials Science*, 2020, 114: 100688.
- [3] Cooke S, Ahmadi K, Willerth S, et al. Metal additive manufacturing: technology, metallurgy and modelling [J]. *Journal of Manufacturing Processes*, 2020, 57: 978-1003.
- [4] Powell D, Rennie A E W, Geekie L, et al. Understanding powder degradation in metal additive manufacturing to allow the upcycling of recycled powders [J]. *Journal of Cleaner Production*, 2020, 268: 122077.
- [5] Katancik M, Mirzababaei S, Ghayoor M, et al. Selective laser melting and tempering of H13 tool steel for rapid tooling applications [J]. *Journal of Alloys and Compounds*, 2020, 849: 156319.
- [6] Chouhan A, Aggarwal A, Kumar A. A computational study of porosity formation mechanism, flow characteristics and solidification microstructure in the L-DED process [J]. *Applied Physics A*, 2020, 126(11): 833.
- [7] Vilardell A M, Krakhmalev P, Fredriksson G, et al. Influence of surface topography on fatigue behavior of Ti6Al4V alloy by laser powder bed fusion [J]. *Procedia CIRP*, 2018, 74: 49-52.
- [8] Qiu Y, Zhang F Y, Hu T T, et al. Effect of laser power on microstructure and hardness of Ti40 flame-retardant titanium alloy deposited by laser cladding on TC4 surface [J]. *Chinese Journal of Lasers*, 2019, 46(11): 1102011.
邱莹, 张凤英, 胡腾腾, 等. 激光功率对 TC4 表面熔覆 Ti40 阻燃钛合金组织及硬度的影响 [J]. *中国激光*, 2019, 46(11): 1102011.
- [9] Qin L Y, Wu J B, Wang W, et al. Microstructures and fatigue properties of Ti-6Al-2Mo-2Sn-2Zr-2Cr-2V titanium alloy fabricated using laser deposition manufacturing [J]. *Chinese Journal of Lasers*, 2020, 47(10): 1002008.
钦兰云, 吴佳宝, 王伟, 等. 激光增材制造 Ti-6Al-2Mo-2Sn-2Zr-2Cr-2V 钛合金组织与疲劳性能研究 [J]. *中国激光*, 2020, 47(10): 1002008.
- [10] Liao C H, Zhou J, Shen H. Electrochemical corrosion behaviors before and after laser polishing of additive manufactured TC4 titanium alloy [J]. *Chinese Journal of Lasers*, 2020, 47(1): 0102003.
廖聪豪, 周静, 沈洪. 增材制造 TC4 钛合金在激光抛光前后的电化学腐蚀性能 [J]. *中国激光*, 2020, 47(1): 0102003.
- [11] Józwick J, Ostrowski D, Milczarczyk R, et al. Analysis of relation between the 3D printer laser beam power and the surface morphology properties in Ti-6Al-4V titanium alloy parts [J]. *Journal of the Brazilian Society of Mechanical Sciences and Engineering*, 2018, 40(4): 215.
- [12] Qi Z J, Zhang X X, Wang Y Y, et al. Effect of B on microstructure and tensile properties of laser additive manufactured TC4 alloy [J]. *Chinese Journal of Lasers*, 2020, 47(6): 0602002.
齐振佳, 张晓星, 王豫跃, 等. 硼对激光增材制造 TC4 微观组织及力学性能的影响 [J]. *中国激光*, 2020, 47(6): 0602002.
- [13] Zhan Y, Liu C, Zhang J J, et al. Measurement of residual stress in laser additive manufacturing TC4 titanium alloy with the laser ultrasonic technique [J]. *Materials Science and Engineering A*, 2019, 762: 138093.
- [14] Zhu Y Y, Tang H B, Li Z, et al. Solidification behavior and grain morphology of laser additive manufacturing titanium alloys [J]. *Journal of Alloys and Compounds*, 2019, 777: 712-716.
- [15] Gu D D, Zhang H M, Chen H Y, et al. Laser additive manufacturing of high-performance metallic aerospace components [J]. *Chinese Journal of Lasers*, 2020, 47(5): 0500002.
顾冬冬, 张红梅, 陈洪宇, 等. 航空航天高性能金属材料构件激光增材制造 [J]. *中国激光*, 2020, 47(5): 0500002.
- [16] Zhang B, Liu S Y, Shin Y C. In-process monitoring of porosity during laser additive manufacturing process [J]. *Additive Manufacturing*, 2019, 28: 497-505.
- [17] Todaro C J, Easton M A, Qiu D, et al. Grain structure control during metal 3D printing by high-intensity ultrasound [J]. *Nature Communications*,

- 2020, 11(1): 142.
- [18] Kistler N A, Corbin D J, Nassar A R, et al. Effect of processing conditions on the microstructure, porosity, and mechanical properties of Ti-6Al-4V repair fabricated by directed energy deposition [J]. *Journal of Materials Processing Technology*, 2019, 264: 172-181.
- [19] Liu S Y, Shin Y C. Additive manufacturing of Ti6Al4V alloy: a review [J]. *Materials & Design*, 2019, 164: 107552.
- [20] Cho J Y, Xu W, Brandt M, et al. Selective laser melting-fabricated Ti-6Al-4V alloy: microstructural inhomogeneity, consequent variations in elastic modulus and implications [J]. *Optics & Laser Technology*, 2019, 111: 664-670.
- [21] Zhang X Y, Fang G, Leeflang S, et al. Effect of subtransus heat treatment on the microstructure and mechanical properties of additively manufactured Ti-6Al-4V alloy [J]. *Journal of Alloys and Compounds*, 2018, 735: 1562-1575.
- [22] Kumar P, Prakash O, Ramamurty U. Micro-and meso-structures and their influence on mechanical properties of selectively laser melted Ti-6Al-4V [J]. *Acta Materialia*, 2018, 154: 246-260.
- [23] Cao S, Chen Z E, Lim C V S, et al. Defect, microstructure, and mechanical property of Ti-6Al-4V alloy fabricated by high-power selective laser melting [J]. *The Journal of The Minerals, Metals & Materials Society*, 2017, 69(12): 2684-2692.
- [24] Iebba M, Astarita A, Mistretta D, et al. Influence of powder characteristics on formation of porosity in additive manufacturing of Ti-6Al-4V components [J]. *Journal of Materials Engineering and Performance*, 2017, 26(8): 4138-4147.
- [25] Walker K F, Liu Q, Brandt M. Evaluation of fatigue crack propagation behaviour in Ti-6Al-4V manufactured by selective laser melting [J]. *International Journal of Fatigue*, 2017, 104: 302-308.
- [26] Zhang X Y, Zhao Y Q, Bai C G. Titanium alloy and applications [M]. Beijing: Chemical Industry Press, 2005: 62-63.
张喜燕, 赵永庆, 白晨光. 钛合金及应用 [M]. 北京: 化学工业出版社, 2005: 62-63.
- [27] Guan Z Z. Laser processing technology manual [M]. Beijing: China Metrology Publishing House, 1998: 240-241.
关振中. 激光加工工艺手册 [M]. 北京: 中国计量出版社, 1998: 240-241.

Adjusting of Al Additions on Microstructures and Properties of TC4 Alloys Fabricated by Laser Additive Manufacturing

Ge Lucheng, Zhao Zisong, Liu Ningxia, Liang Yanpeng, Zhang Jingtao, Wang Cunshan^{*}

Key Laboratory of Materials Modification by Laser, Ion, and Electron Beams, Dalian University of Technology, Dalian, Liaoning 116024, China

Abstract

Objective In recent years, many advances have been made on TC4 alloys, which have received significant attention in the research field of laser additive manufacturing (LAM) owing to their high specific strength, excellent corrosion resistance, and good biocompatibility. However, these alloys have been fabricated without considering the specific characteristics of LAM technology. Consequently, several metallurgical defects, such as pores, inadequate fusion, and cracks, can easily be produced during the LAM process owing to their high metallurgical defect sensitivity. Moreover, metastable phases are often formed locally because of a combination of an alloy's low structural stability and the layer-by-layer nature of the fabrication process. This, in turn, affects the uniformity of mechanical properties, which cannot be completely achieved by optimizing the LAM processing parameters. The main characteristic of the LAM process is that the alloy undergoes the entire process from melting to solidification within a very short time. To effectively control this process, the LAM alloys must possess not only high mechanical, chemical, and tribological properties but also good formability because good formability is associated with characteristics such as high liquid-state fluidity, weak defect sensitivity, and low microsegregation. Therefore, regulating the structure and properties of TC4 through alloying is of great significance. In this work, new alloys were designed based on a basic TC4 composition alloyed with different Al additions. Then, these new alloys were prepared by applying LAM on a TC4 substrate. In addition, a systematic study of the microstructure and properties of

these alloys system was performed with the aim to comprehensively improve the mechanical, chemical, tribological, and forming properties of TC4 alloys through composition optimization.

Methods Alloy design in this work was based on the compositional analysis of a TC4 alloy and the specific characteristics of LAM technology. Then, LAM was employed to fabricate the alloys on a TC4 alloy substrate. The microstructure of as-deposited alloys was investigated using X-ray diffraction (XRD), scanning electron microscopy (SEM), and transmission electron microscopy (TEM). The hardness of these alloys was measured using a Vickers hardness tester. Compressive tests were performed using a universal testing machine. Their tribological properties were evaluated using a wear tester. Further, their electrochemical behavior in an HCl solution was investigated using an electrochemical workstation and their surface roughness was examined using a laser scanning confocal microscope.

Results and Discussions a) The microstructures of all as-deposited alloys exhibited the morphological characteristics of a basket weave, where a multitude of individual α -Ti laths were separated by a thin layer of retained β -Ti (Fig. 2). In these structures, the α -Ti content gradually increased with an increase in Al addition, whereas their size initially decreased with the increase in Al addition (mass fraction) to 1.5% and then increased. This is due to the stabilizing effect of Al on the α -Ti phase and the variation of solidification interval. Moreover, the c/a axial ratio of α -Ti phase gradually increased with the increase in Al addition, indicating that the Al substitution of the Ti atoms exhibits a preference to occur at the $\{1100\}$ α -crystal plane. b) The hardness (Fig. 5) and strength (Table 2) increased with the increase in Al addition owing to the enhanced solution strengthening and increased α -Ti phase, while the ductility (Table 2) reached its highest value at 1.5% Al addition (mass fraction), resulting from the formation of the first α -Ti phase. c) Under dry sliding friction and wear conditions, the wear mechanism of the as-deposited alloys was abrasive wear (Fig. 9). By increasing the Al addition, both the antifriction property and wear resistance gradually increased because the increased hardness effectively enhanced the resistance to abrasive wear (Fig. 8). d) The corrosion surfaces of all the as-deposited alloys exhibited etched-structure characteristics owing to electrode corrosion between the α - and β -Ti phases (Fig. 11). The corrosion resistance initially increased with the Al addition up to 1.5% and then decreased. This is mainly attributed to the changes in the content and size of the α -Ti phase. e) The surface roughness initially decreased and then increased with the increase in Al addition. Its lowest value was obtained at 1.5% Al addition (Fig. 12). This is mainly due to the fluidity and wettability variation of the melted alloy.

Conclusions The microstructures of as-deposited alloys with different Al additions exhibit a basket-weave morphology, where a multitude of individual α -Ti laths are separated by a thin layer of retained β -Ti. In these structures, the content of the α -Ti phase gradually increases with the increase in Al addition, whereas its size initially decreases and then increases. Its lowest value is obtained at 1.5% Al addition. Thus, the hardness, yield strength, and tribological properties of as-deposited alloys increase, while the ductility, corrosion resistance, and surface roughness reach their optimal values at 1.5% Al addition. These results suggest that as-deposited alloys with a 1.5% Al addition exhibit the best combination of mechanical, tribological, chemical, and forming properties, which are superior to those obtained from as-deposited TC4 alloys.

Key words laser technique; laser additive manufacturing; TC4 alloy; composition adjusting; microstructure; property

OCIS codes 140.3390; 160.3900; 140.3380